Thermoelectric properties of Mn substituted synthetic tetrahedrite

Journal:	*Physical Chemistry Chemical Physics*
Manuscript ID:	CP-ART-09-2014-004039.R1
Article Type:	Paper
Date Submitted by the Author:	05-Nov-2014
Complete List of Authors:	MALLIK, RAMESH; INDIAN INSTITUTE OF SCIENCE, PHYSICS Chetty, Raju; Indian Institute of Science, Physics D S, Prem; Indian Institute of Science, Physics Rogl, Gerda; University of Vienna, Institute of Physical Chemistry Rogl, Peter; University of Vienna, Institute of Physical Chemistry Bauer, Ernst; Vienna University of Technology, Institute of Solid State Physics Michor, Herwig; Vienna University of Technology, Institute of Solid State Physics Suwas, Satyam; Indian Institute of Science, Department of Materials Engineering Puchegger, Stephan; University of Vienna, Giester, Gerald; University of Vienna, Institute of Mineralogy and Crystallography

Thermoelectric properties of Mn substituted synthetic tetrahedrite

Raju Chetty[1], Prem Kumar D S.[1], Gerda Rogl[2,6], Peter Rogl[2,6], Ernst Bauer[3,6], Herwig Michor[3], Satyam Suwas[4],Stephan Puchegger[5] ,Gerald Giester[7] and Ramesh Chandra Mallik[*,1]

[1] *Department of Physics, Indian Institute of Science, Bangalore 560012, India*
[2] *Institute of Physical Chemistry, University of Vienna, Währingerstrasse 42, A-1090 Wien, Austria*
[3]*Institute of Solid State Physics, Vienna University of Technology, Vienna, Austria*
[4]*Department of Materials Engineering, Indian Institute of Science, Bangalore 560 012, India*
[5] *Faculty Center for Nanostructure Research, University of Vienna, Boltzmanngasse 5, A-1090 Wien, Austria*
[6]*Christian Doppler Laboratory for Thermoelectricity, Vienna University of Technology, Vienna, Austria*
[7]*Institute of Mineralogy and Crystallography, University of Vienna, Althanstraße 14, A-1090 Vienna, Austria*

Abstract

Tetrahedrite compounds $Cu_{12-x}Mn_xSb_4S_{13}$ ($0 \leq x \leq 1.8$) were prepared by solid state synthesis. A detailed crystal structure analysis of $Cu_{10.6}Mn_{1.4}Sb_4S_{13}$ was performed by single crystal X-ray diffraction (XRD) at 100, 200 and 300 K confirming the noncentrosymmetric structure (space group $I\bar{4}3m$) of a tetrahedrite. The large atom displacement parameter of the Cu2 atoms was described by splitting the 12e site into a partially and randomly occupied 24g site (Cu22) in addition to the regular 12e site (Cu21), suggesting a mix of dynamic and static off-plane Cu2 atom disorder. Rietveld powder XRD pattern and Electron Probe Micro Analysis revealed that all the Mn substituted samples showed a single tetrahedrite phase. The electrical resistivity increased with increasing Mn due to substitution of Mn^{2+} on the Cu^{1+} site. The positive Seebeck coefficient for all samples indicates that the dominant carriers are holes. Even though, the thermal conductivity decreased as a function of increasing Mn, the thermoelectric figure of merit *ZT* decreased, because the decrease of the power factor is stronger than the decrease of the thermal conductivity. The maximum $ZT = 0.76$ at 623 K is obtained for $Cu_{12}Sb_4S_{13}$. The coefficient of thermal expansion $13.5 \pm 0.1 \times 10^{-6}$ K^{-1} is obtained in the temperature range from 460 K to 670 K for $Cu_{10.2}Mn_{1.8}Sb_4S_{13}$. The Debye temperature, $\Theta_D = 244$ K for $Cu_{10.2}Mn_{1.8}Sb_4S_{13}$, was estimated from an evaluation of the elastic properties. The effective paramagnetic moment 7.45 μ_B/f.u for $Cu_{10.2}Mn_{1.8}Sb_4S_{13}$ is fairly consistent with a high spin $3d^5$ ground state of Mn.

*Corresponding author *Email:* rcmallik@physics.iisc.ernet.in

Tel.: +91 8022932450; fax: +91 8023602602.

1. Introduction

Thermoelectric (TE) materials are among the emerging materials for renewable energy sources because of their environmental friendliness. The conversion of heat into electricity using TE materials is primarily based on the Seebeck effect. The material dependent conversion efficiency of TE materials depends on the parameters of the dimensionless figure of merit, defined by $ZT = (S^2/\rho\lambda_T)\mathrm{T}$, where S, ρ, T and λ_T represent the Seebeck coefficient, electrical resistivity, absolute temperature and total thermal conductivity, respectively. The latter is composed of the carrier (λ_C) and the lattice contribution (λ_L). Tetrahedrites ($Cu_{10}Tr_2Sb_4S_{13}$, Tr = Mn, Fe, Co, Ni, Cu, Zn) are a new class of thermoelectric materials consisting of environmentally friendly elements Copper and Sulfur. Tetrahedrites, generally fulfill the thermoelectric (TE) material requirements to achieve a good thermoelectric figure of merit (ZT) because of the following reasons: (1) they have a complex crystal structure with a large number of atoms per unit cell which causes phonon scattering resulting in a low thermal conductivity, and (2) tetrahedrites have a high symmetric crystal structure (cubic) and therefore a high degeneracy of electronic band maxima, leading to an improvement of the power factor. The crystal structure of the mineral tetrahedrite was first determined by Pauling and Neumann (1934) as a derivative of the sphalerite structure. Wuensch (1964) later confirmed the structure from a least squares refinement [1]. Johnson et al. (1986, 1988) proposed a general structural formula for the tetrahedrite minerals denoted as ${}^{[IV]}M1_6\,{}^{[III]}M2_6\left[{}^{[III]}X\,{}^{[IV]}Y_3\right]_4{}^{[VI]}Z$ [where M (l) = Cu, Fe, Zn, Mn, Hg, Cd; M(2) = Cu, Ag; X : Sb, As, Bi, Te; Y and Z = S, Se; superscripts represent the coordination number] in which M1 is occupied by one third of divalent and two third of monovalent atoms at the tetrahedral site, M2 is occupied by monovalent atoms at the trigonal planar site and X is occupied by the semimetals at the pyramidal site. Y and Z are occupied by chalcogen atoms at the tetrahedral and octahedral sites, respectively [2, 3]. In the parent compound $Cu_{12}Sb_4S_{13}$, Cu1 atoms occupy the 12d sites tetrahedrally coordinated by S1 atoms whereas Cu2 atoms are located at the 12e site trigonally coordinated by two S1 and one S2 atoms. The Sb atoms occupy the tetrahedral site coordinated by three S1 atoms, with resulting triangles forming a pyramid. It was described in Refs. [2, 3] that transition metal atoms can be accommodated in natural mineral tetrahedrites. Therefore, Suekuni et al. studied TE properties of synthetic tetrahedrite materials $Cu_{10}Tr_2Sb_4S_{13}$ (Tr = Mn, Fe, Co, Ni, Cu, and Zn) up to 340 K and achieved a maximum $ZT = 0.15$ at 340 K for a Ni substituted tetrahedrite, mainly due to a large Seebeck coefficient and a low thermal conductivity [4]. Later, Lu et al. proposed that natural tetrahedrite can be used as high temperature TE materials; they obtained the maximum ZT close to unity at 723 K for $Cu_{12-x}(Zn, Fe)_xSb_4S_{13}$ (x = 0.5 for Zn and x = 1.0 for Fe) [5]. Again, Suekuni et al. studied high temperature TE properties of Ni substituted tetrahedrites by varying the Ni composition. These studies showed a decrease of the electronic thermal conductivity, reaching a maximum $ZT = 0.7$ at 665 K for x = 1.5 in $Cu_{12-x}Ni_xSb_4S_{13}$ [6]. Lu et al. reported that randomly chosen natural minerals can be used as raw materials for synthesis; they achieved a maximum ZT near unity at 723 K by mixing the natural mineral tetrahedrite powder with pure elements (Cu,Sb,S) using high energy ball milling [7, 8]. A different approach of substitution was to replace Sb by Te, which tunes the Fermi level in a favorable manner; the highest $ZT = 0.92$ at 723 K was reached for synthetic $Cu_{12}Sb_3Te_1S_{13}$ [9]. Recently, Heo et al. studied transport properties of synthetic tetrahedrites $Cu_{10}Tr_2Sb_4S_{13}$ (Tr = Mn, Fe, Co, Ni, Cu, and Zn) and obtained a $ZT = 0.8$ at 575 K for Tr = Mn, then by optimizing the Mn concentration, a maximum $ZT = 1.13$ was found for x = 1 in $Cu_{12-x}Mn_xSb_4S_{13}$ ($0 \leq x \leq 2$) due to the very low thermal conductivity and a relatively high power factor [10].

In the present investigations, the authors selected Mn as doping element to optimize the power factor as well as decreasing thermal conductivity thorough reducing the carrier thermal conductivity which has been motivated by the earlier reports of transition metal elements as dopants (e.g. Zn, Fe, Ni) [5-6]. It is mainly focused on studying the influence of Mn substitution in tetrahedrites on structural as well as transport properties such as electrical resistivity, Seebeck coefficient and thermal conductivity. Here we report on a change of power factor affected by the modification of electrical resistivity and Seebeck coefficient by the substitution of Mn^{2+} on the Cu^{1+} resulting in a reduction of *ZT*. A detailed crystallographic analysis of a compound with nominal composition $Cu_{10.6}Mn_{1.4}Sb_4S_{13}$ is presented using temperature dependent single crystal XRD. Not only high ZT values and high thermal-electric conversion efficiencies η are required for TE generators but also the material's response to thermal and mechanical stresses, generated by in-service conditions of a thermoelectric device, is very important. This was the reason to study the magnetic susceptibility of a compound with higher content of Mn as well as thermal expansion and mechanical properties.

2. Experimental Details

$Cu_{12-x}Mn_xSb_4S_{13}$ (x = 0, 0.5, 1.0, 1.5, 2.0) compounds were prepared by a melting and annealing method following a procedure described in the literature [6]. The starting materials Cu, Mn, Sb, and S with high purity (5N) were weighed in a stoichiometric ratio into a quartz ampoule and sealed under vacuum (~10^{-4} mbar). Then the quartz ampoules were slowly heated to 973 K, held at that temperature for 3 hours and then cooled to 823 K for 30 hours. Then the furnace was switched off to cool down to room temperature. The resulting samples were ground into powder and shaped into pellets by cold pressing. These cold pressed pellets were annealed at 773 K for 30 hours in evacuated quartz tubes. The annealed samples were re-ground, loaded into graphite dies with a diameter of 14 mm, and then hot pressed at a pressure of ~ 30 MPa under a dynamic vacuum at 823 K for 2 hours. The relative densities of the hot-pressed samples were determined using Archimedes' principle (measured densities) reaching >95% for all samples. Cylindrical samples were cut into discs with 6.0 mm diameter and a thickness of 0.5 mm for thermal conductivity measurements, and into cuboids (~11.0 × ~3.0 × ~3.0) for Seebeck and electrical resistivity measurements, respectively.

Single crystals of $Cu_{10.6}Mn_{1.4}Sb_4S_{13}$ suitable for crystal structure analysis were obtained via mechanical fragmentation (in a WC-mortar) of an as cast and annealed alloy with nominal composition $Cu_{10}Mn_2Sb_4S_{13}$ (composition from Electron probe microanalysis (EPMA): $Cu_{10.6}Mn_{1.4}Sb_4S_{13}$). Single crystal X-ray diffraction data at 300 K (and also at 200 and 100 K, cooled by a continuous stream of nitrogen gas enclosing the crystal at a preset temperature) were collected on a four-circle Nonius Kappa diffractometer equipped with a CCD area detector and monochromated MoK_{α}-radiation. For the crystal structure solution and refinement, the program Oscail [11, 12] has been used and the program Structure Tidy [13] was applied for subsequent standardization. Powder X-ray diffraction (XRD) patterns of all samples were collected on a Rigaku Smart Lab instrument using Cu K_{α} radiation after hot pressing. Rietveld refinement was carried out for the crystallographic phase identification using the Fullprof software [14]. Electron probe microanalysis (EPMA) (JEOL JXA-8530F wavelength dispersive spectrometry (WDS)) was carried out for the hot-pressed samples using elemental standards.

Electrical resistivities and Seebeck coefficients were measured between 300 K and 723 K by an ULVAC-RIKO ZEM-3 system. Thermal conductivity which is related by $\lambda_T = D d_s C_p$ where D is thermal diffusivity, d_s is the density of sample and C_p is the specific of heat of the sample. was obtained from an ANTER Flashline 3000 unit in the temperature range between 423 K and 723 K. Thermal diffusivity and specific heat of sample measured by using the equipment ANTER Flashline 3000 unit. The specific heat (C_p) can be measured by placing the standards sample (steel or graphite) with known specific heat, which places next to the sample. The specific heat of the sample can be calculated by using the following formula

$$C_{p,s} = \frac{d_r L_r C_{p,r} \Delta T_r}{d_s L_r \Delta T_s}$$

where $C_{p,r}$ and $C_{p,s}$ are the heat capacities, L_r and L_s are the thickness, of the reference and the specimen, respectively, and ΔT is the temperature increase by laser heating.

The measurement errors for the electrical resistivity and the Seebeck coefficient are 5 % and 10 % for the thermal conductivity. Thermal expansion was measured in the temperature range of 430 K to 660 K with a dynamic mechanical analyser DMA7 (Perkin Elmer Inc.); for details see ref. [15]. Resonant ultrasound spectroscopy (RUS) developed by Migliori et al. [16] was used to determine the elastic properties via the Eigen frequencies of the sample and knowing the sample's mass and dimensions (for details see refs. [17, 18]). A superconducting quantum interference device (SQUID) was employed for the determination of the magnetization from 3 K up to 300 K in fields of 0.1, 1 and 3 T on a 15.38 mg piece.

3. Results and Discussion

3.1 Crystal structure of $Cu_{10.6}Mn_{1.4}Sb_4S_{13}$

The dimensions of the unit cell and a careful inspection of the extinction conditions led to the diffraction symbol *m*3*mI*--- consistent with the description of the structure of a tetrahedrite $Cu_{12}Sb_4S_{13}$[1]. Similar to the results obtained by Wuensch[1], structure refinement of $Cu_{10.6}Mn_{1.4}Sb_4S_{13}$ (in a first attempt with isotropic temperature factors) revealed five crystallographically independent sites in space group $I\bar{4}3m$ (Cu1 in 12d, Cu2 in 12e, S1 in 24g, S2 in 2a, Sb in 8c), where from the Cu2 atom exhibited a large atom displacement parameter (ADP). Also the ADP of Cu1 looked slightly enhanced but was reduced to acceptable levels by inserting Mn into this site in terms of a random distribution of 0.76 Cu1 + 0.24 Mn. The effect is small due to the small difference in atom X-ray scattering power between Cu and Mn atoms and due to the small amount of replacement. The amount of Mn inserted was taken from the electron microprobe analysis (EPMA) of the sample from which the single crystal specimen was extracted. Final refinement with anisotropic thermal parameters for all atoms yielded physically sound ADP parameters for almost spherical atom shapes except for a rather elongated thermal ellipsoid in the Cu2-site. Results of the refinement at room temperature (RT) are listed in Table 1. Whereas each Cu1/Mn atom is tetrahedrally surrounded by S1 atoms (d_{Cu1-S1} = 0.2343 nm) with tetrahedral bond angles of 110.9° (only a marginal deviation from the angles in a regular tetrahedron = 109°28'), the Cu2-atom is trigonally planar coordinated by two S1 and one S2 atoms (d_{Cu2-S1}=0.2245 nm and d_{Cu2-S2}=0.2268 nm). The four atoms (Cu2-S1-S1-S2) are located in a symmetry plane to which the Cu2-ADP ellipsoid shows a strong perpendicular thermal motion (see Fig. 1). The long axis of the ADP-ellipsoid for Cu2 is well in line with the two opposing and neighboring Sb-atoms at a distance of 0.3422 nm from the Cu2-centre. Refinements of the data sets collected at 200 K and 100 K essentially reflected the same features for ADP's and bonding distances (see Table 1). This result is so far consistent with a Synchrotron powder diffraction study of $Cu_{11}Ni_1Sb_4S_{13}$ [6]. Whereas Pfitzner et al. [19] used a Gram-Charlier inharmonic description of the ADP's for Cu atoms in synthetic $Cu_{12}Sb_4S_{13}$, a neutron powder diffraction to elucidate the role of Fe in natural sulfosalts of tetrahedrite $(Cu_{1-x}Fe_x)_{12}Sb_4S_{13}$ and tennantite $(Cu_{1-x}Fe_x)_{12}As_4S_{13}$ [20] revealed that the triangular 12e site is split into a flat pyramidal 24g site situated on both sides of the S1-S1-S2 triangle. The distance among the split atoms was reported to be ~0.06 to 0.07 nm decreasing slightly with increasing Fe-content. Furthermore, the neutron data unambiguously located the Fe-atoms in the tetrahedral 12d sites, consistent with the crystallographic description of $Cu_{10}Tr_2Sb_4S_{13}$ in the literature (T is a 3d metal Mn to Zn [4-10]). Temperature dependent synchrotron data (298 K, 523 K) confirmed little residual electron density between the two randomly occupied Cu2 half filled sites in tetrahedrite ($d_{Cu2-Cu2}$=0.06 nm). This density increases only slightly with temperature [21]. In this context it is interesting to note that a room temperature X-ray single crystal study of an Fe-tennantite proved the presence of a split Cu2 site ($d_{Cu2-Cu2}$=0.0791 nm 28% of the Cu) in addition to Cu2 in the regular trigonal planar 12e site (78% of the Cu) [22].

Assuming a static rather than a dynamic solution for the large ADP of Cu2 in $Cu_{10.6}Mn_{1.4}Sb_4S_{13}$, we allowed a split of the 12e site into a partially and randomly occupied 24g site (Cu22) in addition to the regular 12e site (Cu21). The refinement converged to a slightly lower R-value with about 25% Cu21 covering electron density between the Cu22 atoms at a distance $d_{Cu21-Cu22}$=0.030 nm and $d_{Cu22-Cu22}$=0.045 nm. Crystallographic data are summarized in Table 1. The thermal ellipsoid reduced its long axis by a factor of about 2 but still significant anisotropy remained suggesting a mix of dynamic and static off-plane Cu2 atom disorder. Consequently the Cu2 atom vibrates in a low energy mode perpendicular to the trigonal sulfur plane. Such low energy modes of a loosely bound atom in cages of skutterudites and clathrates are believed to be beneficial in scattering heat-carrying phonons. Assuming a fairly independent Einstein oscillation for Cu2-U22, the characteristic Einstein temperature $\Theta_{E,ii}$ can be derived from equation (1). Similarly the ADP's of the framework atoms can be used to estimate the Debye temperature Θ_D of the solid employing equation (2). Least squares fits as a function of temperature of the ADP's (see Fig.2) for Cu2 employing the Einstein model (Eq.(1)) and the Debye model (Eq.(2) for the framework atoms)

$$U_{ii} = \frac{h^2}{2mk_B\Theta_{E,ii}} coth\frac{\Theta_{E,ii}}{2T} + d^2 \tag{1}$$

$$U_{iso} = \frac{3h^2T}{mk_B\Theta_D^2}\left[\frac{T}{\Theta_D}\int_0^{\Theta_D/T}\frac{x}{e^x - 1}dx + \frac{\Theta_D}{4T}\right] + d^2 \tag{2}$$

(where $\Theta_{E,ii}$ is the Einstein temperature; ii refers to the direction or plane of the vibration; m is the mean atomic mass; k_B is the Boltzmann constant; $\hbar$ is the reduced Planck constant, d is a disorder parameter and Θ_D is the Debye temperature) result in $\Theta_{E,11}$ = 84 K, $\Theta_{E,22=33}$ = 40 K and Θ_D = 220 K. The disorder parameter from the Einstein function was d=0.026 nm in fine agreement with the static displacement of 0.030 nm obtained from the refinement of the Cu2 split in 3 particles Cu21 and Cu22 (see above). As noted earlier [19-22] the Cu2-atom inclines to attain a tetrahedral coordination but needs to dislocate in direction of repulsive Sb-neighbours.

3.2 Powder XRD

The present work discussed on the quantitative information of powder XRD using the Rietveld refinement and evaluated the lattice parameters for all the samples in comparison to the ref.10 because the behavior of the lattice parameters as function of doping content gives the idea about the substitution of Mn on the Cu content and the Rietveld refinement of powder XRD gives a phase confirmation of the prepared compound. Powder XRD pattern of all samples are shown in figure 3and all peaks are indexed to the cubic tetrahedrite phase $Cu_{12}Sb_4S_{13}$ (ICSD#25707) following the structure model derived from the X-ray single crystal study of $Cu_{10.6}Mn_{1.4}Sb_4S_{13}$. Figure S1 in the supporting information shows the maximum intensity peak of all the samples related to the (222) plane and it is observed that, there is a systematic peak shift towards a lower Bragg angle (2θ) with increase in the substitution of Mn on the Cu site. This shift confirms the increase of lattice spacing. Rietveld refined powder XRD patterns revealed tetrahedrite as the main phase for all the samples, only for the compound $Cu_{12}Sb_4S_{13}$ shown in figure 4, the presence of a small amount of Cu_3SbS_4 (~1.7%) as a secondary phase was confirmed. Lattice parameters obtained from the Rietveld refinement for all the samples are plotted in figure 5 as a function of the Mn content. A systematic increase and the linear behavior of the lattice parameter as a function of the Mn content confirm the substitution of Mn on the Cu1 site (12d site) due to the substitution of larger ionic-radius-element Mn^{+2} (0.066 nm) for the smaller ionic radius element Cu^{+} (0.060 nm) [23]. The lattice parameters in the present work are in good agreement with the literature data for the end member compounds ($Cu_{12}Sb_4S_{13}$ - $Cu_{10}Mn_2Sb_4S_{13}$) [4, 24].

3.3 Microstructure and phase characterization

In comparison to the ref.10, the present work explains the microstructure, phase purity and actual composition of the prepared samples which can influence the transport properties. Fractured surface secondary electron images of ESEM with X 2000 magnification for all the hot pressed samples is shown in Figure S2 (supporting information). The surface morphology of all the samples showed homogeneous and continuous large grain growth, which indicates the compaction of the hot pressed samples. The morphology of the samples with $x_{Mn} = 0$ and $x_{Mn} = 0.4$ are well compacted without observation of porosity, whereas for the samples with $x_{Mn} > 0.4$, a small amount of porosity is observed, which indicates less density as compared to the former samples. This is in good agreement with the measured density of the hot pressed samples. The SEM images of all samples showed large grains with simple microstructure without noticeable shape or any oriented features. It was observed that, there are no changes in the microstructure with increasing Mn content, which indicates that no affect on thermal conductivity from the microstructure contribution was expected. Back-scattered electron micrographs of EPMA with a magnification of X 2000 for all the samples after hot pressing is shown in figure S3 (supporting information). The parent compound showed a small amount of Cu_3SbS_4 in addition to the tetrahedrite phase, which is confirmed by the XRD measurement. No impurity phases were detected in all the Mn substituted compounds $Cu_{12-x}Mn_xSb_4S_{13}$, which is in agreement with the XRD data. The composition of all samples was analyzed by EPMA (WDS), revealing a slight loss of the volatile Mn during sample preparation. The comparison between the nominal and EPMA compositions is shown in table 2.

3.4 *Transport properties*

3.4.1 Electrical resistivity

Temperature dependent electrical resistivity for all the samples is shown in figure 6. The resistivity of $Cu_{12}Sb_4S_{13}$ tetrahedrite and Mn substituted compounds $Cu_{12-x}Mn_xSb_4S_{13}$ (x=0.4 and 0.9) with a low content of Mn is slightly increasing with increasing temperature, referring to a metallic or heavily doped semiconductor behavior. In contrary to these observations, the resistivity of Mn substituted samples $Cu_{12-x}Mn_xSb_4S_{13}$ (x = 1.4 and 1.8) with a higher content of Mn showed a negative temperature dependence suggesting semiconducting behavior. Recently, Lu *et al.* reported that pure synthetic tetrahedrite $Cu_{12}Sb_4S_{13}$ shows a metal like p-typed conductivity from DFT (Density Functional Theory) band structure calculations [5]. Generally, a complete filling of the valence bands in the compound occurs and yields semiconducting behavior, when the Cu atoms exist in both the Cu^{1+} and Cu^{2+} oxidation states and balance the charge neutrality in the form of $Cu_{10}^{1+}Cu_2^{2+}Sb_4^{3+}S_{13}^{2-}$. In case all the copper is in the Cu^{1+} state,

$Cu_{12}Sb_4S_{13}$ has more carriers (2 holes) than $Cu_{10}Mn_2Sb_4S_{13}$ when Mn is Mn^{+2} (or Mn = Zn). The electrical resistivities of $Cu_{12}Sb_4S_{13}$ and samples with a low Mn content are in the same order of magnitude (~10^{-3} Ω-cm) as reported for Zn substituted tetrahedrites [5]. However, the electrical resistivity is systematically increasing with the Mn substitution in the compounds $Cu_{12-x}Mn_xSb_4S_{13}$ (x = 0, 0.4, 0.9, 1.4 and 1.8). The reason is the filling of valence bands by introducing additional electrons with an increasing substitution of Cu^{1+} by Mn^{2+} atoms. This substitution leads to a reduction of the carrier concentration, resulting in an increase of the electrical resistivity. This is evidenced by an increase of ρ from 1.013 mΩ-cm for $Cu_{12}Sb_4S_{13}$ to 1.693 mΩ-cm and 3.313 mΩ-cm at room temperature (RT) for samples with x = 0.4 and x = 0.9 respectively. As the Mn content approached x = 1.4 and 1.8, the resistivity at RT increases by one and two orders of magnitude higher in comparison to $Cu_{12}Sb_4S_{13}$. Thermal activation energies E_a for the temperature dependent electrical resistivity of a semiconductor are estimated using the formula

$$\rho = \rho_0 e^{E_a/k_B T} \qquad (3)$$

where ρ_0 is a pre-exponential factor, E_a is the thermal activation energy, k_B is Boltzmann's constant. The values of activation energies 22.66 meV and 52.69 meV are determined from the slope, E_a/k_B, obtained by plotting the logarithm of resistivity, ln (ρ), as function of the inverse temperature, 1/T, for the compounds with x = 1.4 and 1.8, respectively. The inset of figure 8 shows the ln (ρ) versus 1/T for $Cu_{10.2}Mn_{1.8}Sb_4S_{13}$. The increase of activation energy from the sample with x = 1.4 to the sample with x = 1.8 clearly indicates that more energy is needed for carriers to jump from the acceptor level to the valence band in case of the sample with x = 1.8 compared to that with x = 1.4. A similar type of behavior, i.e. increasing of resistivity with increase of the transition metal substitution (Zn, Ni and Mn) has been reported earlier for the synthetic tetrahedrite [5, 6, 10]. A difference in the magnitude of electrical resistivity for all the samples is observed as compared to the ref.10, which may be due to variation in the carrier concentration and this can be influenced by the presence native point defects and/or the amount of doping content (actual composition).

3.4.2 Seebeck coefficient

Seebeck coefficients as a function of temperature for all the compounds are shown in figure 7. The positive Seebeck coefficient for all the samples in the temperature range studied indicates that holes are the dominant charge carriers. Following a similar trend as the electrical resistivity, the increase in the Seebeck coefficient with the Mn content is due to the significant reduction of carrier concentration resulting from a shift of the Fermi level near to the top of the valence band as reported earlier [5, 6, 10]. This can be explained by using the equation of the Seebeck coefficient for the p-type semiconductors [25]

$$S = \frac{k_B}{e}\left[\frac{E_F - E_v}{k_B T} + A_v\right] \tag{4}$$

where A_v is a constant, E_F is the Fermi energy, E_v is top of the valance band energy, k_B is the Boltzmann constant and T is the absolute temperature. From equation (4), the Seebeck coefficient increases with the increase of the E_F-E_v value, which is affected by the position of the Fermi level. As the Mn content is increasing, the position of the Fermi level shifts towards the top of the valence band and comes close to the intrinsic energy level of the band gap. All this happens because the holes in the valence bands are filled with additional electrons created through the substitution of Mn^{2+} on Cu^{1+} sites. Therefore, the shift of the Fermi level near to the intrinsic level causes the value E_F-E_v to increase, which results in the increase of the Seebeck coefficient with the rise of Mn content from 90 μV/K for the unsubstituted compound to 96 μV/K and 111 μV/K at RT for samples with x = 0.4, 0.9, respectively. The increase of S values for compounds with the lower Mn content is less, which is in good agreement with the resistivity data. As the Mn content increased with x = 1.4 and 1.8, the S value at RT increased by 2 and 3 times of higher magnitude in comparison to the unsubstituted compound $Cu_{12}Sb_4S_{13}$. A similar type of behavior namely increasing of S with a transition metal (Zn, Ni and Mn) substituted synthetic tetrahedrite material was reported in the literature [5, 6, 10]. The Seebeck coefficient of all samples increased with increasing temperature as reported in [5, 6, 10]. The Seebeck coefficient value is exceeding 300 μV/K at high temperature for the compound $Cu_{10.2}Mn_{1.8}Sb_4S_{13}$, which is even higher than the literature value of 247 μV/K at 575 K [10] for the Mn end member of tetrahedrite. The difference in the Seebeck coefficient values in the present work and literature may be due to the variation in the carrier concentration.

For better understanding the effect of doping on electrical properties, estimation of carrier concentration at room temperature is attempted using Hall effect and it is unsuccessful due to the difficulty in making contacts for the measurement. Earlier, Lu et al. reported that the attempts in the measurement of carrier concentration for Fe and Zn substituted tetrahedrite were also unsuccessful. Hence, carrier concentration is roughly estimated using the Mott's formula by

$$S_d(T > \theta_D) = \frac{\pi^2 k_B^2 2m_e}{e\hbar^2 (3n\pi^2)^{2/3}} T \qquad (5)$$

with m_e being the carrier mass, e the carrier charge, k_B the Boltzmann constant, ħ the Planck's constant, T the temperature, and n the charge carrier density, respectively. The carrier concentration values estimated using the room temperature Seebeck coefficient are in the range between 5×10^{20} cm^{-3} for x=0 to 9×10^{19} for x=1.8 cm^{-3} in $Cu_{12-x}Mn_xSb_4S_{13}$. This gives the partial evidence for the decrease of resistivity with increase of Mn conent.

3.4.3 Power factor

Figure 8 shows the temperature dependent power factor (PF) for all the samples. With increasing the Mn content, the power factor systematically decreased mainly as a consequence of a significant increase in the electrical resistivity with increase of the Mn content. The maximum power factor, 17 μW/cm-K^2 at 623 K, is obtained for the compound $Cu_{12}Sb_4S_{13}$, due to the low electrical resistivity (1.17×10^{-3} Ω-cm) and the moderate Seebeck coefficient (142 μV/K). It should be noted that this power factor is about three times higher than the power factor for $Cu_{12}Sb_4S_{13}$ reported by Heo et al. [10]. Caused by larger values of Seebeck coefficients and low resistivities, the power factor of the Mn substituted compounds with $0.5 \leq x \leq 1.4$ even surpass the highest power factor (PF) values reported in the literature [10]. Although, it was intended to optimize the power factor by varying the Mn content, but the PF is systematically decreased with Mn content, which is mainly effected by the increase of electrical resistivity. The difference of power factor values for all the compounds in the present work and literature [10] stems from the variations in the Seebeck coefficients and electrical resistivities. This may be due to the variation the carrier concentration which can be influenced by the changes in the actual composition of the prepared compounds or by presence of some native point defects.

3.4.4 Thermal conductivity

Figure 9 displays the temperature dependent total and lattice thermal conductivity. The total thermal conductivity is slightly increasing with increasing temperature with values less than 15 mW/cm-K in the entire temperature range for all the samples, which is similar to the reported data [5, 6, 9]. The total thermal conductivity decreases with an increase of the Mn content attributed to the reduction of the carrier thermal conductivity, λ_C. λ_C can be calculated from the Wiedemann-Franz relation $\lambda_C = LT/\rho$, where L is Lorenz number. The value of Lorenz number can be obtained by using the following formula [26]

$$L = \left(\frac{k_B}{e}\right)^2 \left(\frac{(r+7/2)F_{r+5/2}(\eta)}{(r+3/2)F_{r+1/2}(\eta)} - \left[\frac{(r+5/2)F_{r+3/2}(\eta)}{(r+3/2)F_{r+1/2}(\eta)}\right]^2 \right) \tag{6}$$

To find the correct L value, the reduced Fermi energy η has to be calculated by using the Seebeck coefficient values measured from the following relation

$$S = \pm \frac{k_B}{e} \left(\frac{(r+5/2)F_{r+3/2}(\eta)}{(r+3/2)F_{r+1/2}(\eta)} - \eta \right) \tag{7}$$

where $F_n(\eta)$ is the n−th order Fermi integral, $F_n(\eta) = \int_0^\infty \frac{\chi^n}{1+e^{\chi-\eta}} d\chi$, $\eta = \frac{E_F}{k_B T}$, k_B is the Boltzmann constant, e the electron charge and E_F the Fermi energy. By assuming acoustic phonon scattering (r =−1/2) as the main carrier scattering mechanism, the Lorenz number can be calculated by substituting the values of η and r into equation (6). The Lorenz number value decreased with increase of temperature and reaches the value from ~1.98 $\times 10^{-8}$ WΩK^{-2} at RT to ~1.79 $\times 10^{-8}$ WΩK^{-2} at 723 K for the unsubstituted tetrahedrite and from ~1.54 $\times 10^{-8}$ WΩK^{-2} at RT to ~1.51 $\times 10^{-8}$ WΩK^{-2} at 723 K for the highest Mn content. The lattice thermal conductivity ($\lambda_L = \lambda_T - \lambda_C$) can be evaluated by subtracting λ_C from λ_T. The lattice contribution to the total thermal conductivity increased with increasing Mn content up to the samples with x = 0.9 as a consequence of the decrease of carrier contribution, resulting in a decreasing interaction of the heat carrying phonons with charge carriers.. For the samples x = 1.4 and 1.8, the total as well as the lattice thermal conductivity are almost the same, which is due to the negligible contribution from the carrier thermal conductivity and the effect of Mn in the tetrahedrite. The lattice thermal conductivity values are obtained in the range of 4-8 mW/cm-K for the compounds $Cu_{12-x}Mn_xSb_4S_{13}$ ($0 \leq x \leq 1.8$). These low values of λ_L are mainly due to the complex crystal structure consisting of a large number of atoms (58 atoms per unit cell) with random distribution of the transition metals as well as by the dynamic and static off-plane Cu2 atom disorder. A large value of the Grüneisen parameter, a characteristic of lattice anharmonicity leads to enhanced phonon scattering [5, 6]. It is interesting to note that, although total thermal conductivity values in the present work decreased with increase of Mn content and reached the value from 12.5 mW/cm-K at 423 K for $Cu_{12}Sb_4S_{13}$ to 6.4 mW/cm-K at 423 K for $Cu_{10.2}Mn_{1.8}Sb_4S_{13}$, the reported values [10] decrease from ~11 mW/cm-K at 475 K for $Cu_{12}Sb_4S_{13}$ to ~1.8 mW/cm-K at 475 K for $Cu_{10}Mn_{2.0}Sb_4S_{13}$. As mentioned by Heo et al. [10] that thermal conductivity depends on the method of sample preparation and measurement technique. Also thermal conductivity of a material depends on the thermal diffusivity (D), density (d) and specific heat (C_p) is related by $\lambda = D \times d \times Cp$. From this relation, thermal conductivity is also depends on the density of sample. If the density of the sample is less, it leads to increase in the porosity of the sample which is related by $\lambda = \lambda_0 (1 - P^{2/3})$ where λ_0 is thermal conductivity of material having no pores and P is the pores fraction in the material. From this relation, thermal conductivity of a material decreases with increasing of pores due to the increase of phonon scattering at pores. The difference of thermal conductivity values in the present work and the literature may be due to the variation in the method of sample preparation and samples density [88% from the literature, >95% in the present work].

3.4.5 Thermoelectric figure of merit (*ZT*)

The temperature dependent thermoelectric figure of merit (*ZT*) is shown in figure 10. The maximum $ZT = 0.76$ at 623 K is obtained for the pure synthetic tetrahedrite $Cu_{12}Sb_4S_{13}$ and is higher than the reported data of 0.30 at 575 K [10]. This result is mainly attributed to the large power factor of 17 μW/cm-K^2 at 623 K whereas the literature value is only 5.62 μW/cm-K^2 at 575 K. A significant reduction of the power factor occurred with increasing Mn content, which is mainly affected by the increased electrical resistivity by the substitution of Mn^{2+} for Cu^{1+}. Although the total thermal conductivity is suppressed with increasing Mn content, a systematic decrease in *ZT* is obtained, which is affected by the decreased power factor with Mn substitution in tetrahedrite. Even though, the power factor value of 7.73 μW/cm-K^2 at 573 K for the compound $Cu_{11.1}Mn_{0.90}Sb_4S_{13}$ is higher than the reported value of 5.36 μW/cm-K^2 at 575 K [10], in the present work thermal conductivity value of 10.8 mW/cm-K at 573 K is much higher than the value of 2.7 mW/cm-K at 575 K reported by Heo et al. [10]. Consequently *ZT* = 0.41 at 573 K is lower in comparison with the literature value of 1.13 at 575 K for $Cu_{11}Mn_{1.0}Sb_4S_{13}$ [10]. As compared to the transport properties of present work and ref.10 for compound with nominal composition $Cu_{10}Mn_2Sb4S_{13}$ at 575 K, the electrical resistivity (66 mΩ-cm in the present work, 27mΩ-cm in ref.10) and Seebeck coefficient (328 μV/K in the present work, 247 μV/K in ref.10) is higher. This could be due to the variation in the carrier concentration which is result of either the presence of native defects and/or the amount of doping content (actual composition). Thermal conductivity (0.61 W/m-K in t in the present work, 0.17 W/m-K in ref.10) of $Cu_{10}Mn_2Sb_4S_{13}$ at 575 K is high as compared to the ref.10, which could be due to the large difference in the samples density (>95% present work, 88% ref 10). The lattice thermal conductivity of reported samples are much lower than the present study samples because of more porosity which is responsible for higher ZT. In conclusion, the large difference in the *ZT* between the present work and literature is mainly due to the variation in the power factor and thermal conductivity. The existence of low thermal conductivity values in the literature for Mn substituted tetrahedrite may arise from the low sample density (88%).

3.5 Thermal expansion coefficient of $Cu_{10.2}Mn_{1.8}Sb_4S_{13}$

The thermal expansion coefficient α follows from a temperature derivative of the length change,

i.e., $$\alpha = \left(\frac{\partial \Delta \ell}{\partial T}\right)\frac{1}{\ell_0} \qquad (8)$$

where ℓ_0 is the absolute length of the solid, $\Delta\ell$ is the change in length, and ∂T is the temperature difference. The thermal expansion coefficient α was calculated for $Cu_{10.2}Mn_{1.8}Sb_4S_{13}$in the temperature range of 460 to 670 K using equation (7). In this range a strict linearity of $(l-l_0)/l_0$ versus T was observed (see figure 11). With $\alpha = 13.5 \pm 0.2 \text{ x}10^{-6}$ K^{-1} the value is consistent with the literature value of $\alpha \sim 13.4 \times 10^{-6}$ K^{-1} (obtained from the high temperature XRD in the range of 295 to 573 K for the compound $Cu_{12}Sb_4S_{13}$) [19]. In the range of 300 – 400 K, however, a lower thermal expansion coefficient with $\alpha = 9.20 \pm 0.2 \times 10^{-6}$ K^{-1} was calculated. Single crystal XRD data for the compound $Cu_{10.6}Mn_{1.4}Sb_4S_{13}$ revealed a thermal expansion coefficient $\alpha = 9.15 \times 10^{-6}$ K^{-1} in the temperature range of 100 K to 300 K, which is close to the measured and calculated value of $Cu_{10.2}Mn_{1.8}Sb_4S_{13}$ in the range of 300-400 K.

3.6 Elastic properties of $Cu_{10.2}Mn_{1.8}Sb_4S_{13}$

The RUS theory establishes the relation between kinetic energy and elastic energy and hence makes it possible to carry out a least squares fit by minimizing the sum of the squared differences between the measured and calculated Eigen frequencies to derive the elastic properties, i. e. the Young's modulus, E, and the Poisson's ratio, ν.

With E and ν the bulk modulus, B, and the shear modulus, G, were calculated using the relations

$$B = E/(3 - 6\nu) \qquad (9)$$

$$G = E/(2\nu + 2) \qquad (10)$$

The fit of the measured spectrum of the Eigen frequencies of $Cu_{10.2}Mn_{1.8}Sb_4S_{13}$ with a relative density of 98% provided a Young's modulus of $E = 49\pm1$ GPa and a Poisson ratio $\nu = 0.30\pm0.01$. These values differ slightly from the values reported by Fan et al. [27] with $E = 56$ GPa and $\nu = 0.29$. Using equations (9) and (10), the shear modulus with $G = 19\pm1$ GPa and the bulk modulus with $B = 41\pm1$ GPa were calculated. As a consequence from the difference in E and ν also G and B differ slightly from the reported data of G=21.97 GPa and B=44.9 GPa [27]. This slight variation in the elastic properties is due to the difference in the relative density and/or compositional changes.

There are various methods to extract the Debye temperature θ_D from elastic properties. Isotropic compounds prepared from hot pressed fine powders into a dense bulk are suitable for determining θ_D from sound velocity, using Anderson's equation [28]

$$\Theta_D = \frac{h}{k_B}\left(\frac{3nNd}{4M\pi}\right)^{1/3} v_m \qquad (11)$$

where h is the Plank's constant, k_B is the Boltzmann's constant, N is Avogadro's number, d is the density, M is the molecular weight, and n is the number of atoms in the asymmetric unit. The mean sound velocity v_m follows the simplified expression [29]:

$$v_m = \left[\frac{1}{3}\left(\frac{2}{v_T^3} + \frac{1}{v_L^3}\right)\right]^{-1/3} \quad \left[\frac{1}{3}\left(\frac{2}{\mathrm{v}_\mathrm{T}^3} + \frac{1}{\mathrm{v}_\mathrm{L}^3}\right)\right]^{-1/3} \qquad \text{with } v_L = \left(\frac{3B+4G}{3d}\right)^{1/2} \text{ and } v_T = \left(\frac{G}{d}\right)^{1/2}$$

(12)

where v_L and v_T are the longitudinal and transversal sound velocities, respectively.

With equations (10) and (11) the Debye temperature Θ_D = 244 K could be extracted. This value is only slightly higher than that estimated from the temperature dependent X-ray single crystal study (Θ_D = 220 K).

3.7 Magnetic properties of $Cu_{10.2}Mn_{1.8}Sb_4S_{13}$

The temperature dependent magnetic susceptibility, $\chi = M/H$, of $Cu_{10.2}Mn_{1.8}Sb_4S_{13}$ shown in figure 12 as well as the inverse susceptibility, $1/\chi = H/M$, in the inset reveal a local moment Curie-Weiss paramagnetic behavior with a small Pauli-type component. Accordingly, the solid line in the inset of figure 12 displays a fit with a modified Curie-Weiss law, $\chi(T) = \chi_0 + C/(T-\Theta_p)$, where $\chi_0 = 2.3\times10^{-3}$ emu/mol corresponds to a temperature independent Pauli susceptibility. The paramagnetic Curie-Weiss temperature Θ_p = -14.3 K is indicative of antiferromagnetic correlation, and **C** = $N_A\mu_0\mu_{eff}^2/3k_B$ = 6.93 emu K/mol is the Curie constant which is used to calculate the effective paramagnetic moment, μ_{eff} = 7.45 μ_B/f.u. This value of the effective moment is slightly smaller than a theoretical value of 8.0 μ_B/f.u. expected for Mn^{+2} ions being in a $3d^5$ high spin configuration. The moderate reduction of the Mn d-electron moment as compared to the free ion Mn^{+2} value results from hybridization effects. A Mn high spin ground state was also extracted from magnetic susceptibility data for $Cu_{10}Mn_2Sb_4S_{13}$ [10].

4 Conclusion

Synthetic tetrahedrites with Mn substitution were prepared by melting and sintering followed by annealing. The analysis of atomic displacement parameters via single crystal XRD for $Cu_{10.6}Mn_{1.4}Sb_4S_{13}$ reveals that Cu2 atom vibrates in a low energy mode perpendicular to the CuS_3 triangle plane, which is favorable for the suppression of thermal conductivity. Rietveld refined powder XRD and EPMA revealed synthetic tetrahedrite $Cu_{12}Sb_4S_{13}$ as the main phase and a small amount of a secondary Cu_3SbS_4 phase. The lattice parameters obtained from the Rietveld analysis linearly increased with increasing Mn content and confirmed the substitution of Mn on the Cu site. The electrical resistivity increased with increasing Mn content and confirmed the substitution of Mn^{2+} for Cu^{1+}. The positive Seebeck coefficient for all the compounds in the entire temperature range studied indicates that the majority carriers are holes. The Seebeck coefficient follows the trend of the electrical resistivity, it increases with increasing Mn content. The total thermal conductivity decreased with increasing Mn content due to the suppression of the carrier contribution, as well as due to the substitution effect of Mn on the Cu site. The combined effects of power factor and thermal conductivity yielded a maximum ZT= 0.76 at 623 K for the pure synthetic tetrahedrite $Cu_{12}Sb_4S_{13}$. The transport properties are differed as compared to the ref.10 is may be due to the variation in carrier concentration which influences the power factor and the samples density leads to large difference in thermal conductivity. As a result of both the power factor and thermal conductivity leads to a significant difference in ZT in comparison with ref.10. For $Cu_{10.2}Mn_{1.8}Sb_4S_{13}$ the thermal expansion coefficient α is derived, and α =13.5 ± $0.1\text{x}10^{-6}$ K^{-1} is obtained in the temperature range from 460 to 670 K. The Debye temperature, Θ_D = 244 K, is calculated using the elastic properties for the compound $Cu_{10}Mn_2Sb_4S_{13}$ and in the same range with Θ_D = 220 K for $Cu_{10.6}Mn_{1.4}Sb_4S_{13}$ obtained from ADP calculations. The magnetic susceptibility measurement in the low temperature range of 3 K to 330 K for $Cu_{10.2}Mn_{1.8}Sb_4S_{13}$ confirmed Mn in a $3d^5$ high spin configuration.

Acknowledgements

The authors would like to thank the Department of Science & Technology (DST), India for financial support through Grant No INT/AUA/BMWF/P-13/2011 and the OEAD for support via the WTZ Austria-India under grant IN 09/2011. Parts of the work were supported by the Christian Doppler Laboratory for Thermoelectricity.

References

1. B. J. Wuensch, *Z. Kristallogr*, 1964, **119**, 437.
2. N. E. Johnson, J. R. Craig and J. D. Rimstidt, *Can. Mineral* 1986, **24**, 385.
3. N. E. Johnson, J. R. Craig and J. D. Rimstidt, *Am. Miner*, 1988, **73**, 389.
4. K. Suekuni, K. Tsuruta, T. Ariga and M. Koyano, *Appl. Phys Express*, 2012, **5**, 051201.
5. X. Lu, D. T. Morelli, Y. Xia, F. Zhou, V. Ozolins, H. Chi, X. Zhou and C. Uher, *Adv. Energy Mater.*, 2013, **3**, 342-348.
6. K. Suekuni, K. Tsuruta, M. Kunii, H. Nishiate, E. Nishibori, S. Maki, M. Ohta, A. Yamamoto and M. Koyano, *J. Appl. Phys.*, 2013, **113**, 043712.
7. X. Lu and D. T. Morelli, *PCCP*, 2013, **15**, 5762-5766.
8. X. Lu and D. T. Morelli, *MRS Commun.*, 2013, **3**, 129-133.
9. X. Lu and D. Morelli, *J. Electron. Mater.*, 2014, **43**, 1983-1987.
10. J. Heo, G. Laurita, S. Muir, M. A. Subramanian and D. A. Keszler, *Chem. Mater.*, 2014, **26 (6)**, 2047–2051.
11. P. McArdle, K. Gilligan, D. Cunningham, R. Dark and M. Mahon, *CrystEngComm*, 2004, **6**, 303-309.
12. G. Sheldrick, *Acta Crystallogr., Sect. A*, 2008, **64**, 112-122.
13. L. M. Gelato and E. Parthe, *J. Appl. Crystallogr.*, 1987, **20**, 139-143.
14. T.Roisnel and J. Rodriguez-Carvajal, *Mat. Sci. Forum*, 2001, **118**, 378-381
15. G. Rogl, L. Zhang, P. Rogl, A. Grytsiv, M. Falmbigl, D. Rajs, M. Kriegisch, H. Müller, E. Bauer, J. Koppensteiner, W. Schranz, M. Zehetbauer, Z. Henkie and M. B. Maple, *J. Appl. Phys.*, 2010, **107**, 043507
16. A. Migliori and J. D. Maynard, *Rev. Sci. Instrum.*, 2005, **76**, 121301.

17. L. Zhang, G. Rogl, A. Grytsiv, S. Puchegger, J. Koppensteiner, F. Spieckermann, H. Kabelka, M. Reinecker, P. Rogl, W. Schranz, M. Zehetbauer and M. A. Carpenter, *Mater. Sci. Eng., B*, 2010, **170**, 26-31.

18. G. Rogl and P. Rogl, *Sci. Adv. Mater.*, 2011, **3**, 517-538.

19. A. Pfitzner, M. Evain and V. Petricek, *Acta Crystallogr., Sect. B*, 1997, **53**, 337-345.

20. J. Andreasen, E. Makovicky, B. Lebech and S. Møller, *Phys. Chem. Miner.*, 2008, **35**, 447-454.

21. K. Friese, A. Grzechnik, E. Makovicky, T. Balić-Žunić and S. Karup-Møller, *Phys. Chem. Miner.*, 2008, **35**, 455-465.

22. S. Kharbish, G. Giester and A. Beran, *Neues Jahrbuch für Mineralogie - Abhandlungen*, 2010, **187**, 159-166.

23. R. D. Shannon, *Acta Crystallogr., Sect. A*, 1976, **32**, 751-767.

24. N. E. Johnson, *Powder Diffr.*, 1991, **6**, 43-47.

25. H. Fritzsche, *Solid State Commun.*, 1971, **9**, 1813-1815.

26. Y.-L. Pei, J. He, J.-F. Li, F. Li, Q. Liu, W. Pan, C. Barreteau, D. Berardan, N. Dragoe and L.-D. Zhao, *NPG Asia Mater*, 2013, **5**, e47.

27. X. Fan, E. Case, X. Lu and D. Morelli, *J. Mater. Sci.*, 2013, **48**, 7540-7550.

28. O. L. Anderson, *J. Phys. Chem. Solids*, 1963, **24**, 909-917.

29. E. Schreiber, O. L. Anderson and N. Soga, *Elastic Constants And Their Measurements*, Mcgraw-Hill Education, New York, 1974.

Tables

Table 1. X-Ray single crystal data for $Cu_{10.6}Mn_{1.4}Sb_4S_{13}$; space group $I\bar{4}3m$; No. 217 (crystal size: 112x84x70 μm^3, data at various temperatures; redundancy >10; μ_{abs} = 8.23 [mm^{-1}]; U_{ij} in [in 10^{2}nm^2]). Standardized with program Structure Tidy [13].

Parameter/temperature	300 K	300 K	200 K	100 K
	Cu2-atom in split site: C21, Cu22	Cu2-atom in one site	Cu2-atom in one site	Cu2-atom in one site
Formula from refinement	$Cu_{10.6}Mn_{1.4}Sb_4S_{13}$	$Cu_{10.6}Mn_{1.4}Sb_4S_{13}$	$Cu_{10.6}Mn_{1.4}Sb_4S_{13}$	$Cu_{10.6}Mn_{1.4}Sb_4S_{13}$
a [30]	1.03947(2)	1.03947(2)	1.03840(2)	1.03764(2)
Data collection, 2θ range (°)	2≤2θ ≤72.6; 100 sec/frame	2≤2θ ≤72.6; 100 sec/frame	2≤2θ ≤72.0; 100 sec/frame	2≤2θ ≤72.5; 100 sec/frame
Total number of frames	213 for 6 sets, scan width 2°	213 for 6 sets, scan width 2°	236 for 5 sets, scan width 2°	246 for 5 sets, scan width 2°
Reflections in refinement	492≥4σ(F_o) of 535	492≥4σ(F_o) of 535	503≥4σ(F_o) of 535	505≥4σ(F_o) of 533
mosaicity	<0.44	<0.44	<0.45	<0.47
Number of variables	25	18	18	18
$R_F = \Sigma\|F_0-F_c\|/\Sigma F_0$	0.0330	0.0339	0.0341	0.0331
R_{Int}	0.060	0.060	0.060	0.060
wR2	0.089	0.092	0.090	0.091
GOF	1.025	1.053	1.062	1.068
Extinction (Zachariasen)	0.0025(2)	0.0024(2)	0.0008(1)	0.0005(1)
S1 in 24g (x,x,z); occ.	1.00(1)	1.00(1)	1.00(2)	1.00(1)
x, z	x = 0.1154(1), z = 0.3608(1)	x = 0.1154(1), z = 0.3608(1)	x = 0.1156(1), z = 0.3609(1)	x = 0.1156(1), z = 0.3611(1)
$U_{11}=U_{22}$, U_{33} [in 10^{2}nm^2]	0.0183(4), 0.0162(6)	0.0183(4), 0.0161(6)	0.0144(4), 0.0126(6)	0.0107(4), 0.0106(6)
$U_{23}=U_{13}$, U_{12}	0.0012(3), -0.0007(5)	0.0010(3), -0.0006(5)	0.0010(3), -0.0006(5)	0.0005(3), -0.0001(4)
S2 in 2a (0,0,0); occ.	1.00(1)	1.00(1)	1.00(2)	1.00(1)
$U_{11}=U_{22}=U_{33}$; $U_{23}=U_{13}=U_{12}=0$	0.0217(9)	0.0215(9)	0.0186(9)	0.0164(9)
Sb in 8c (x,x,x); occ.	1.00(1)	1.00(1)	1.00(1)	1.00(1)
x	x = 0.26747(3)	x = 0.26748(3)	x = 0.26777(4)	x = 0.26803(4)
$U_{11}=U_{22}=U_{33}$; $U_{23}=U_{13}=U_{12}$	0.0183(2); -0.0021(1)	0.0183(2); -0.0020(1)	0.0143(2); -0.0017(1)	0.0107(2); -0.0013(1)
Cu1 (M1) in 12d (¼,½,0); occ.	0.76(2) Cu + 0.24 Mn	0.76(2) Cu + 0.24 Mn	0.76(2) Cu + 0.24 Mn	0.76(2) Cu + 0.24 Mn
U_{11}; $U_{22} = U_{33}$	0.0263(8); 0.0211(3)	0.0145(2); 0.0120(1)	0.0188(7); 0.0155(3)	0.0130(6); 0.0104(3)
Cu21 in 12e (x,0,0) ; occ.	occ=0.25(1)	1.00(1)	1.00(1)	1.00(1)
x:	0.205(2)	0.2160(2)	0.2165(2)	0.2168(2)
U_{11}, $U_{22}=U_{33}$; U_{23}; $U_{13}=U_{12}=0$	0.010(4); 0.054(11); -0.049(96)	0.0217(8); 0.084(1); -0.055(1)	0.0179(8); 0.069(1); -0.047(1)	0.0155(7); 0.0549(8); -0.038(1)
Cu22 in 24g (x,x,z)	occ= 0.09(1)	-	-	-
x;z:	x = 0.0184(15); z = 0.2193(8)			
$U_{11}=U_{22}$, U_{33}	0.049(4), 0.0195(25)			
$U_{23}=U_{13}$, U_{12}	0.0067(18), -0.026(4)			
Residual density; max; min [e/A³]	0.93 (at Cu1); -0.70	1.0 (0.015 nm from Sb); -0.87	1.39 (0.167 nm from Sb); -0.60	1.04 (0.041 nm from Cu2); -0.66
Principal mean square atomic displacements U	S1 0.0190 0.0187 0.0152	S1 0.0189 0.0185 0.0153	S1 0.0150 0.0147 0.0117	S1 0.0113 0.0108 0.0099
	S2 0.0217 0.0217 0.0217	S2 0.0215 0.0215 0.0215	S2 0.0186 0.0186 0.0186	S2 0.0164 0.0164 0.0164
	Sb 0.0204 0.0204 0.0141	Sb 0.0204 0.0204 0.0142	Sb 0.0159 0.0159 0.0110	Sb 0.0120 0.0120 0.0081
	Cu1 0.0263 0.0211 0.0211	Cu1 0.0259 0.0211 0.0211	Cu1 0.0188 0.0155 0.0155	Cu1 0.0130 0.0104 0.0104
	Cu21 0.0590 0.0492 0.0103	Cu2 0.1383 0.0290 0.0217	Cu2 0.1163 0.0215 0.0179	Cu2 0.0923 0.0156 0.0155
	Cu22 0.0768 0.0240 0.0179			

Interatomic distances for $Cu_{10.6}Mn_{1.4}Sb_4S_{13}$; space group $I\bar{4}3m$; Cu2-atom in one site; standard deviation less than 0.0003 nm

S1 - 1Cu2		0.2268	0.2264	0.2263
- 2Cu1		0.2343	0.2340	0.2337

- 1Sb	**0.2436**	**0.2435**	**0.2436**
S2 - 6Cu2	**0.2245**	**0.2248**	**0.2249**
Sb - 3S1	**0.2436**	**0.2435**	**0.2436**
Cu1- 4S1	**0.2343**	**0.2340**	**0.2337**
Cu2- 1S2	**0.2245**	**0.2248**	**0.2249**
- 2S1	**0.2268**	**0.2264**	**0.2263**

Interatomic distances for $Cu_{10.6}Mn_{1.4}Sb_4S_{13}$; space group $I\bar{4}3m$; Cu2-atom in split site: C21, Cu22; standard deviation less than 0.0003 nm

S1 - 1Cu21	**0.2345**	**S2 - 12Cu22**	**0.2295**	**Cu1 - 4S1**	**0.2343**	**Cu21-Cu22**	**0.0308**	**Cu22-Cu22**	**0.5417**
- 2Cu22	**0.2262**	**Sb - 3S1**	**0.2436**			**-2S1**	**0.2345**	**-S2**	**0.2951**
- 2Cu1	**0.2343**	**- 3Cu22**	**0.3150**			**- 1S2**	**0.2132**	**-2S1**	**0.2262**
- 1Sb	**0.2436**					**- 4Cu22**	**0.2999**	**-2Cu22**	**0.2952**
								-2Cu21	**0.2999**
								-1Sb	**0.3150**

Table 2. Nominal composition, EPMA phase composition and secondary phase for $Cu_{12-x}Mn_xSbS_{13}$ ($0 \leq x \leq 1.8$).

Nominal composition	**EPMA, composition [A]**	**Secondary Phases [B]**
$Cu_{12}Sb_4S_{13}$	$Cu_{12}Sb_4S_{13}$	Cu_3SbS_4
$Cu_{11.5}Mn_{0.5}Sb_4S_{13}$	$Cu_{11.6}Mn_{0.4}Sb_4S_{13}$	
$Cu_{11.0}Mn_{1.0}Sb_4S_{13}$	$Cu_{11.1}Mn_{0.9}Sb_4S_{13}$	
$Cu_{10.5}Mn_{1.5}Sb_4S_{13}$	$Cu_{10.6}Mn_{1.4}Sb_4S_{13}$	
$Cu_{10.0}Mn_{2.0}Sb_4S_{13}$	$Cu_{10.2}Mn_{1.8}Sb_4S_{13}$	

[A] SULFUR IS NORMALIZED TO 13ATOMS PER FORMULA UNIT

[B] DETECTED BY EPMA.

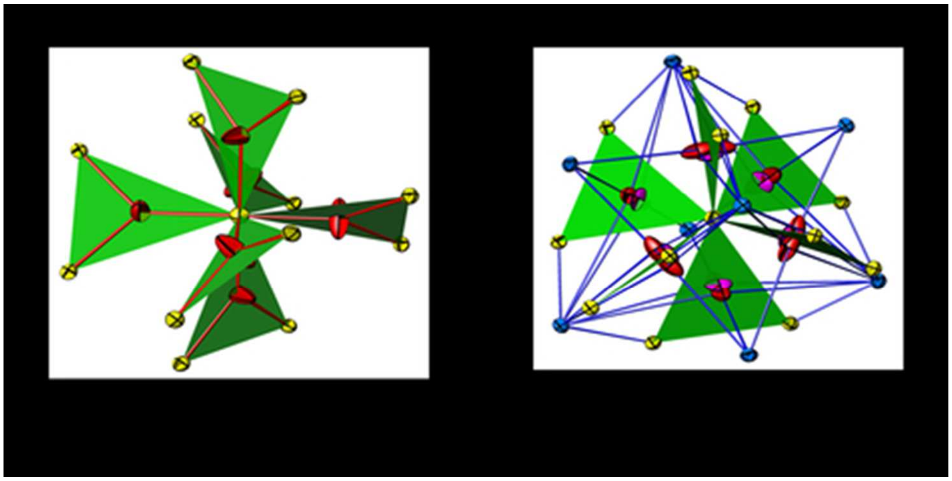

(a) Thermal ellipsoids of Cu2 in the tetrahedrite structure of Cu10.6Mn1.4Sb4S13 perpendicular to the plane S1-S1-S2. Cu2 atoms are octahedrally surrounding the S2 atom in the center. (This figure was called “six-bladed spinner” by Wuensch 1. (b) Thermal ellipsoids of Cu2 (red) in the tetrahedrite structure of Cu10.6Mn1.4Sb4S13 split into partially occupied sites 12e for Cu21 and 24g for Cu22. Cu22 atoms are dislocated out of the S1-S1-S2 plane (yellow atoms S) in direction of repulsive Sb-atoms (blue).
39x19mm (300 x 300 DPI)

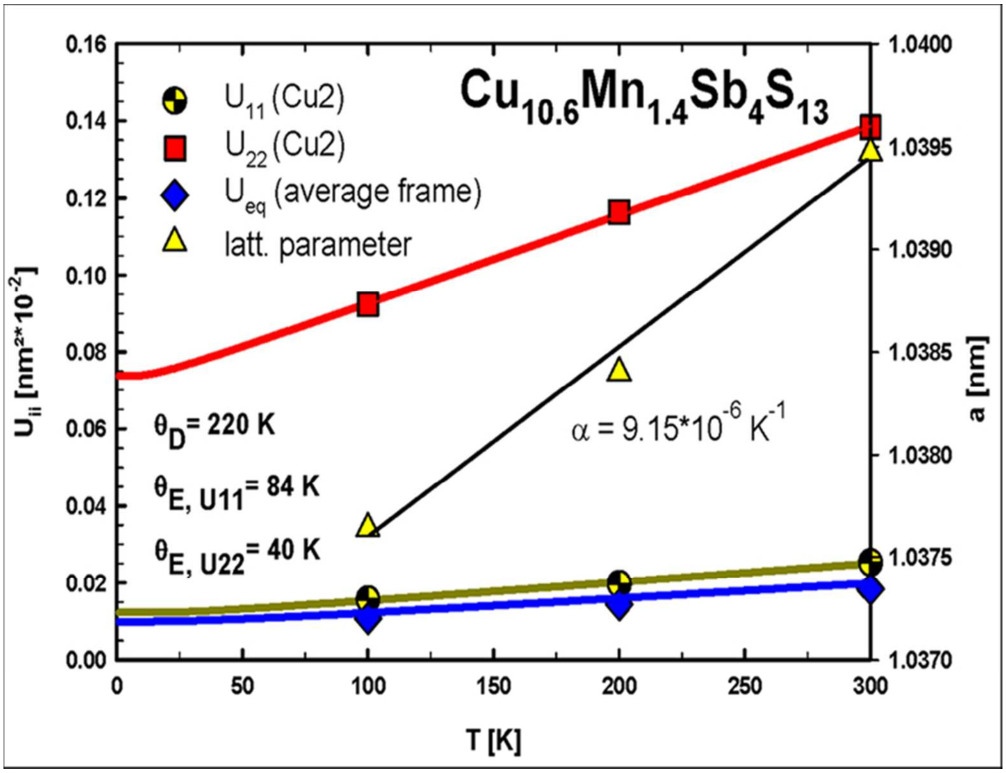

Temperature dependent atomic displacement and lattice parameters of Cu10.6Mn1.4Sb4S13 (Cu2 unsplit in 12e site).
64x49mm (300 x 300 DPI)

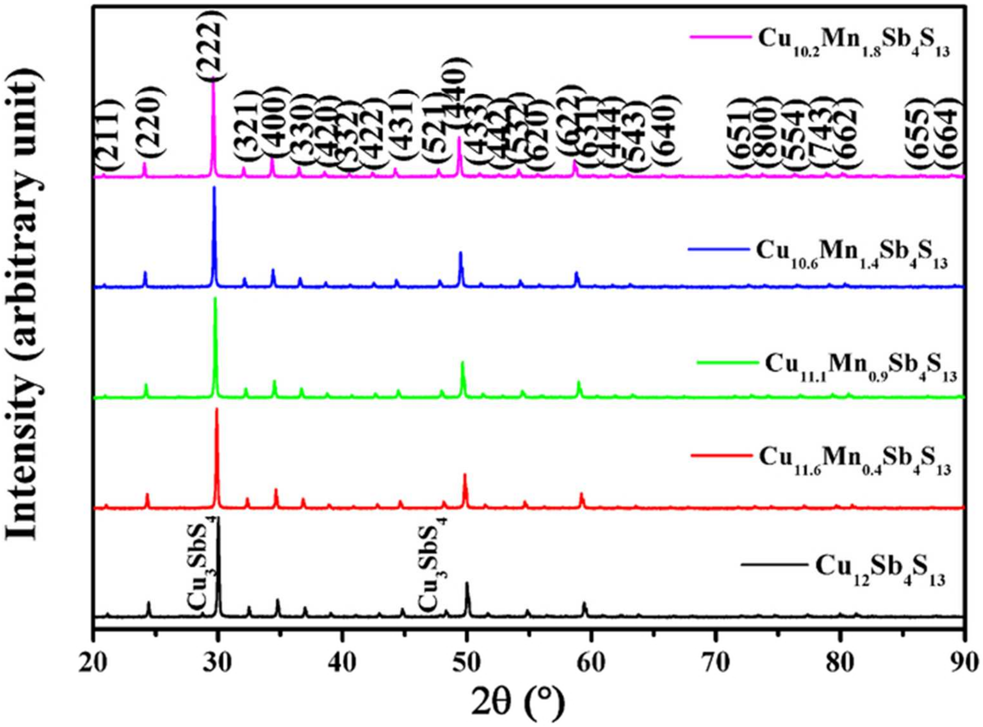

Powder XRD patterns for the compounds Cu12-xMnxSb4S13 (x = 0, 0.4, 0.9, 1.4, 1.8).
62x46mm (300 x 300 DPI)

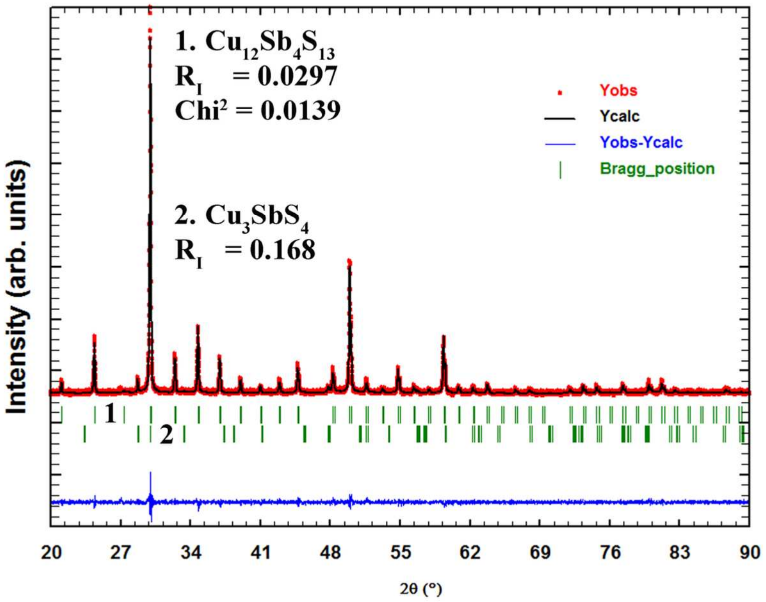

Rietveld refinement powder XRD pattern for Cu12Sb4S13.
63x46mm (600 x 600 DPI)

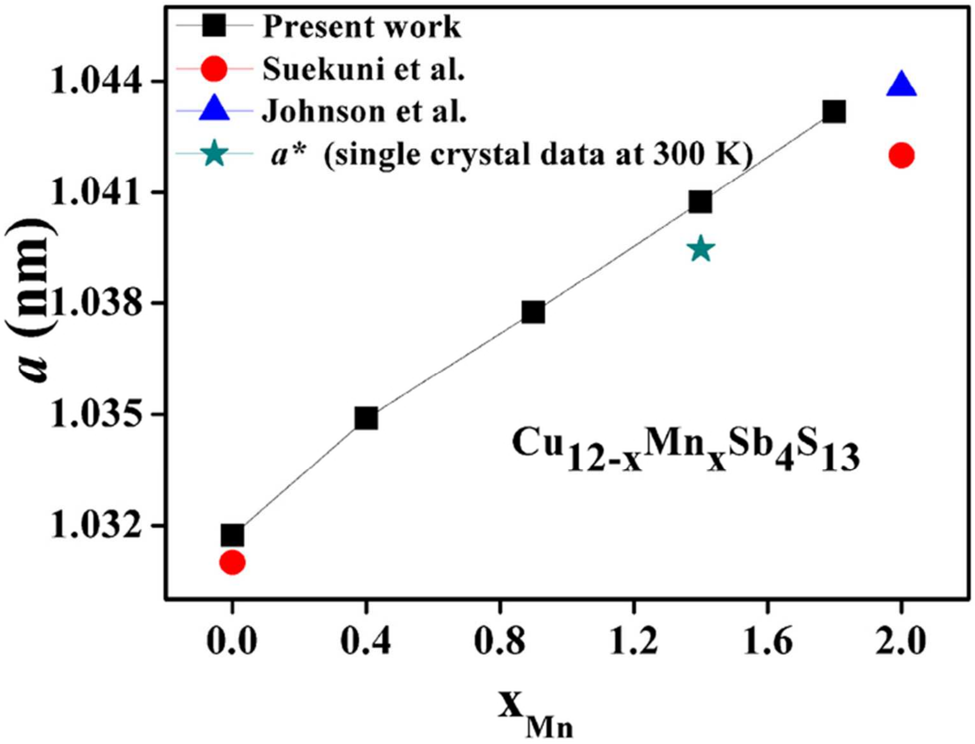

Variation lattice parameter as a function of EPMA Mn content in Cu12-xMnxSb4S13 (x = 0, 0.4, 0.9, 1.4, 1.8).
64x49mm (300 x 300 DPI)

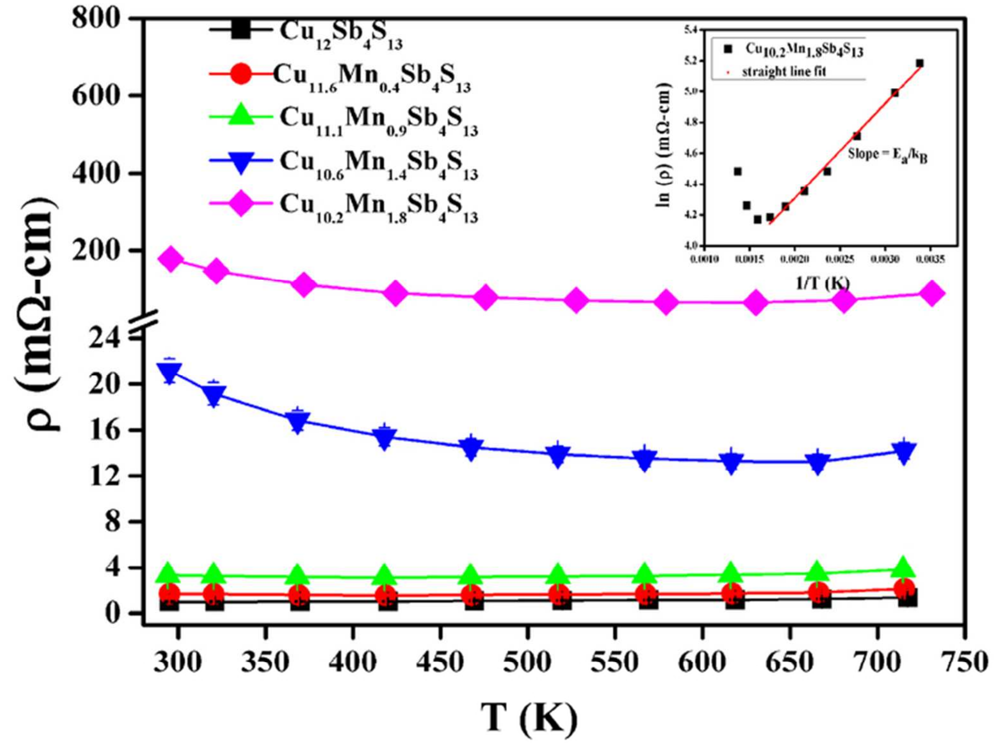

Temperature dependent electrical resistivity for Cu12-xMnxSb4S13 (x = 0, 0.4, 0.9, 1.4, 1.8). Inset figure represents the ln (ρ) versus 1/T for Cu10.2Mn1.8Sb4S13.
64x49mm (300 x 300 DPI)

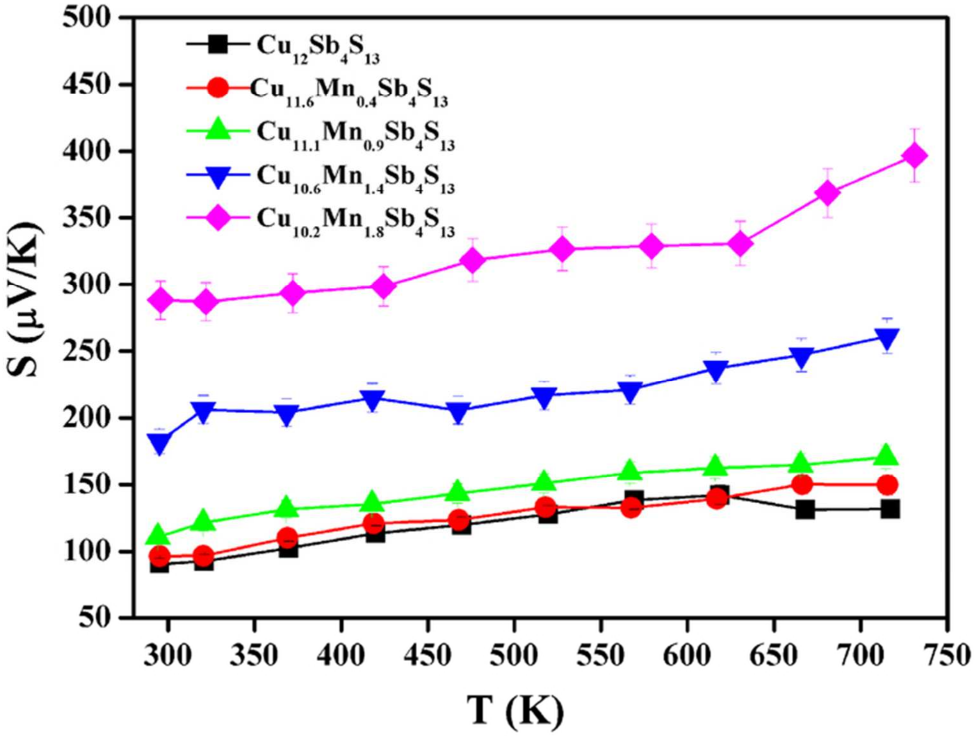

Seebeck coefficient as a function of temperature for Cu12-xMnxSb4S13 (x = 0, 0.4, 0.9, 1.4, 1.8).
64x49mm (300 x 300 DPI)

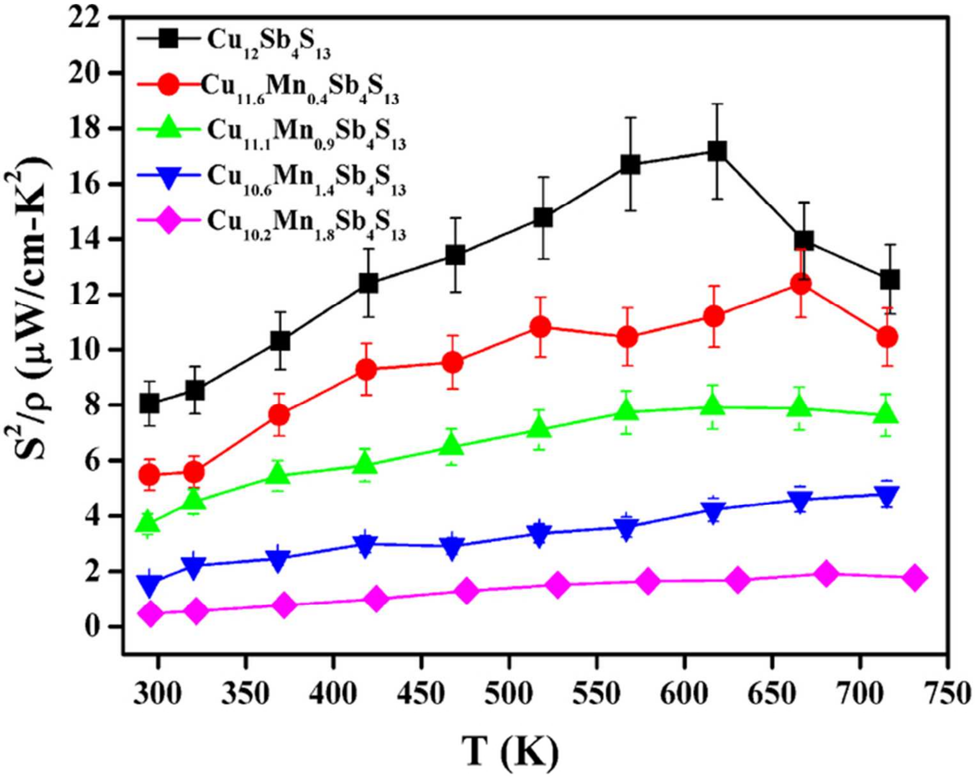

Temperature dependent of power factor for Cu12-xMnxSb4S13 (x = 0, 0.4, 0.9, 1.4, 1.8).
64x51mm (300 x 300 DPI)

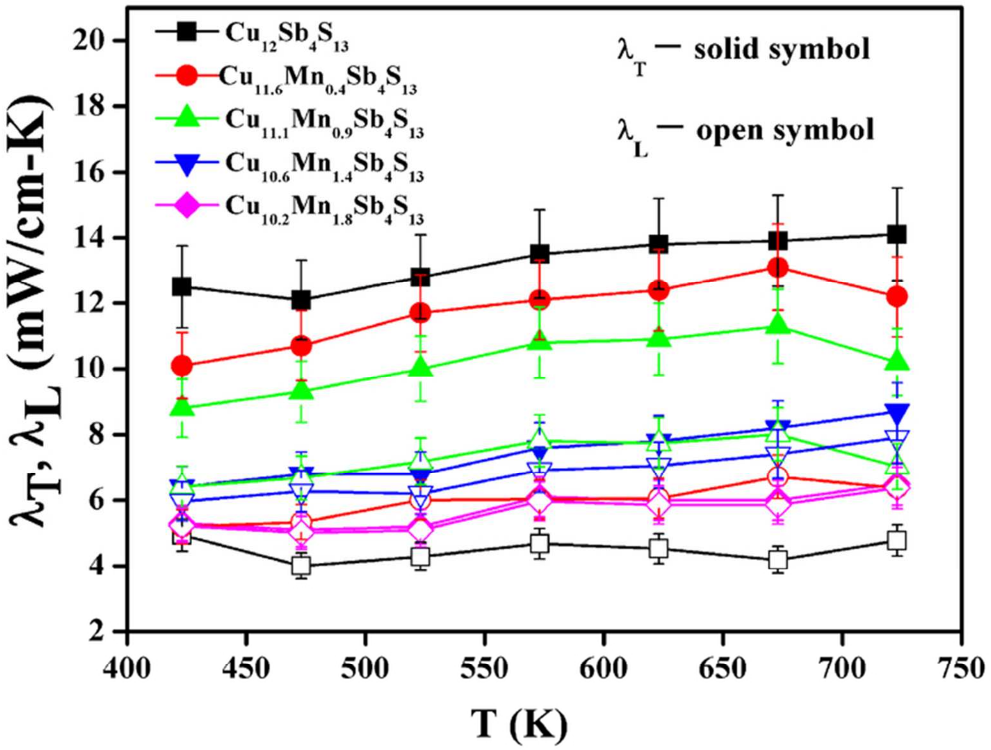

Temperature dependent total (solid symbols) and Lattice (open symbols) thermal conductivity for Cu12-xMnxSb4S13 (x = 0, 0.4, 0.9, 1.4, 1.8).
64x49mm (300 x 300 DPI)

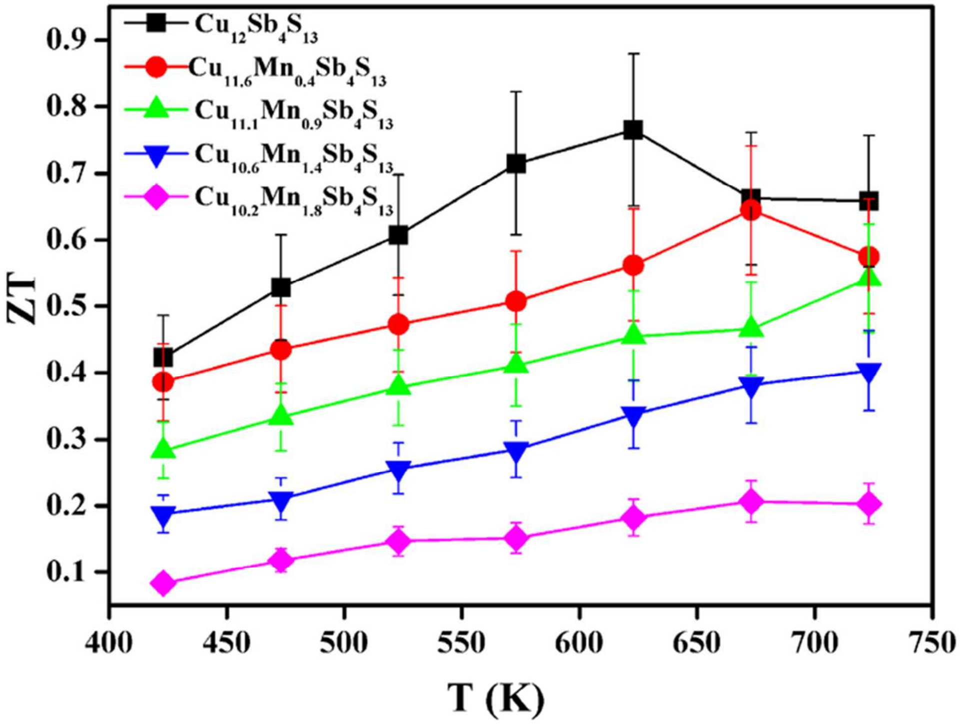

Thermoelectric figure of merit (ZT) as function of temperature for Cu12-xMnxSb4S13 (x = 0, 0.4, 0.9, 1.4, 1.8).
64x49mm (300 x 300 DPI)

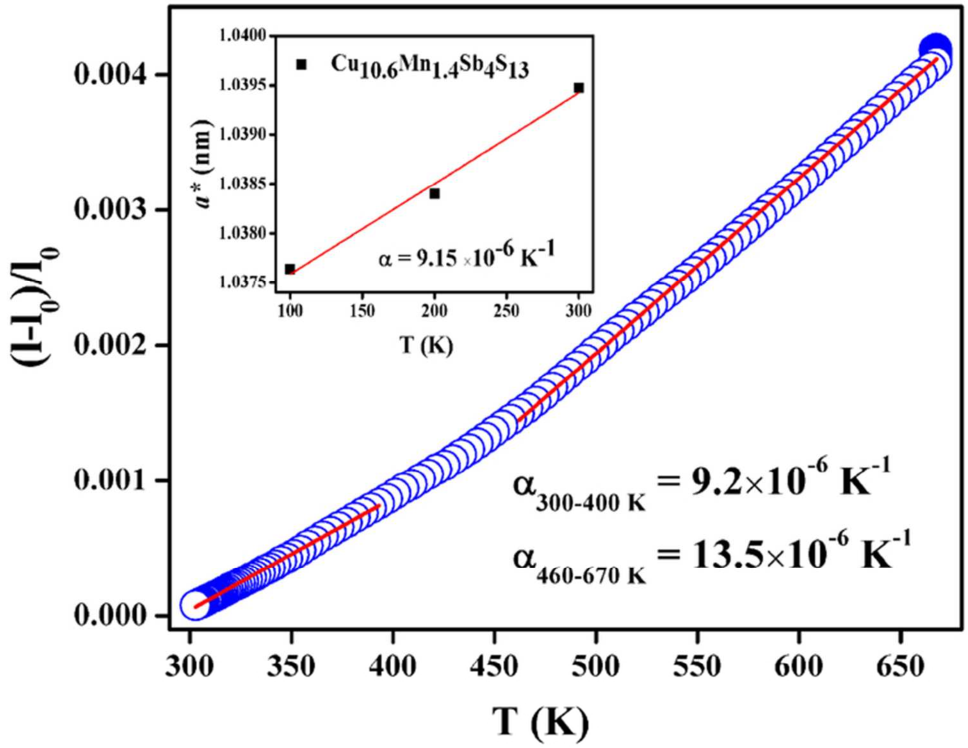

(l-l0)/l0 plot versus temperature for the compound Cu10.2Mn1.8Sb4S13. Insert: lattice parameter vs. T of Cu10.6Mn1.4Sb4S13.
64x49mm (300 x 300 DPI)

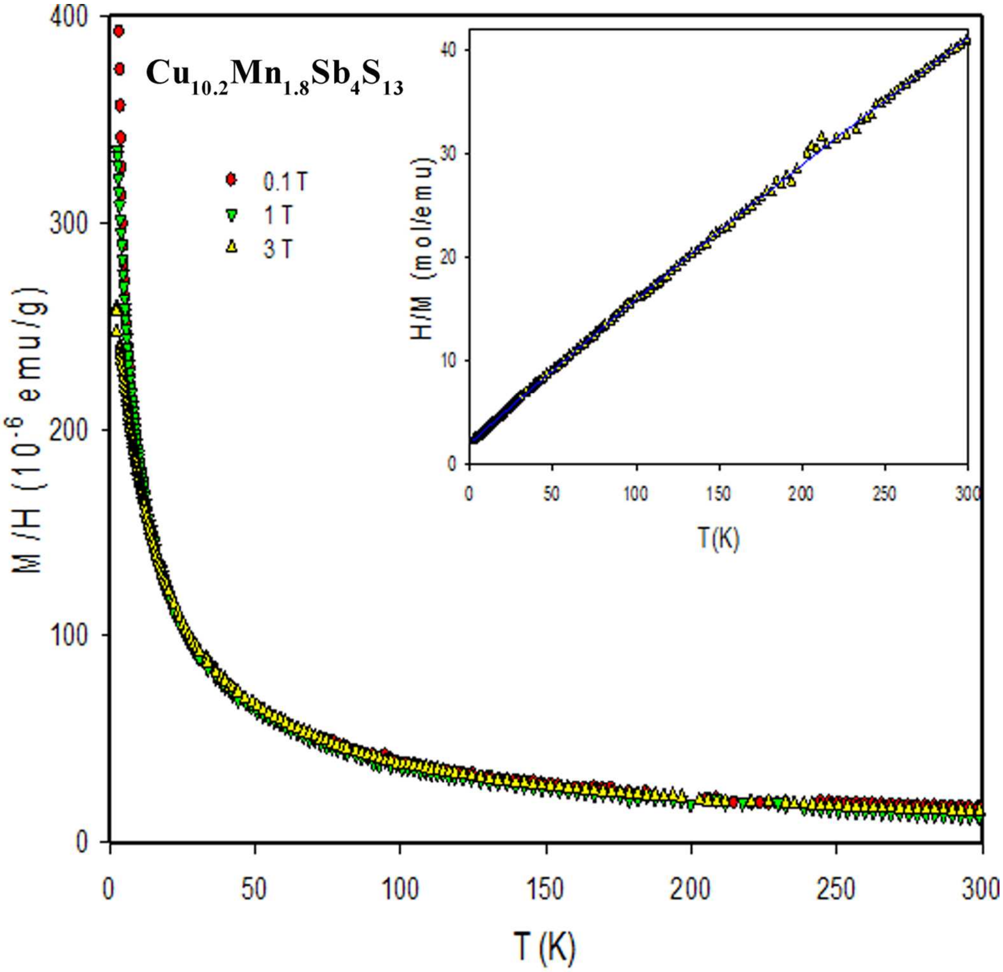

The temperature dependent magnetic susceptibility, χ = M/H, of Cu10.2Mn1.8Sb4S13. Inset figure show the inverse susceptibility, 1/χ = H/M versus temperature. The solid line in the inset of Fig. 12 displays a fit with a modified Curie-Weiss law, χ(T) = χ0 + C/(T-Θp), where χ0 = 2.3×10-3 emu/mol corresponds to a temperature independent Pauli susceptibility.
136x132mm (300 x 300 DPI)